DOI: 10.13009/EUCASS2017-65

7TH EUROPEAN CONFERENCE FOR AERONAUTICS AND AEROSPACE SCIENCES (EUCASS)

DOI: ADD DOINUMBER HERE

Numerical Simulation of Shock Wave/Laminar Boundary Layer Interaction Over a Blunt Geometry

Mahsa Mortazavi⋆ *and Doyle Knight*⋆†
⋆*Rutgers - The State University of New Jersey*
New Brunswick, New Jersey 08903, USA
mahsa.mortazavi89@gmail.com · doyleknight@gmx.com
†Corresponding author

Abstract

Shock wave/boundary layer interaction is an influential phenomenon in all hypersonic aircraft. It creates complex flow structure with extreme localized pressure and heat transfer, which can impose design limitations. Understanding this phenomenon and gaining the ability to predict the flow parameters in such interactions is very crucial. In this study, three dimensional shock wave boundary layer interaction in a laminar hypersonic flow past a cylindrical fin, mounted on a flat plate is numerically investigated and the effect of the sweep angle fin is analyzed. Numerical simulation is conducted using a viscous perfect gas model with an MPI code written in the C++ language by the authors. The results are compared with the experiment for validation. Good agreement of the numerical results with the experimental data validates our calculations.

Introduction

There is a renewed interest in aircraft with speeds ranging from supersonic to hypersonic with increasing funding provided from organizations such as NASA to advance technologies in high speed flights. One of the most dominant phenomenon in hypersonic flights is shock wave boundary layer interaction, due to its extreme effects on the flow structure in addition to pressure and heat transfer on the vehicle. As a result, it is very important to fully understand the physics of this influential occurrence and be able to predict the flow with such interactions using numerical simulations.

The adverse pressure gradient imposed from the shock wave to the boundary layer can separate the boundary layer and create a complex flow structure. A separation shock wave forms over the separated region which interacts with the original shock wave and creates a shock/shock interaction. The effect of the shock wave boundary layer interaction is evident by an increase in the aerothermodynamic loads on the surface of the aircraft. There have been many analytical, experimental and numerical investigation on this interaction. Some examples of these attempts are research conducted by Chantez[4,5] , Bur[3] , Boldyrev[1] , John[11] and Swantek[18] . In their works experimental and numerical simulations have been performed to study the fundamentals of laminar/turbulent transition, real gas effects, heat transfer distributions, the effect of ramped leading edge and many other topics related to shock wave boundary layer interaction.

The effect of the geometric bluntness of the model on the shock wave boundary layer interaction has been studied in many research studies, such as Coet *et al.*[6,7] . They showed that the bluntness of the plate reduces the aerothermodynamic loads due to the reduction of the speed of the flow from hypersonic to supersonic regime at the shock wave boundary layer interaction region. Borovoy *et al.*[2] obtained the same result with the effect of the plate's bluntness on the heat transfer rate at the interaction region due to increase in the separation bubble size and decrease in the gas density in the high-entropy layer. Moreover, they showed that as the radius of the plate's bluntness increases, the heat transfer rate decreases to a certain threshold value for the bluntness radius. They further observed that by increase in freestream Mach number, the threshold value decays and the effect of the bluntness of the plate on the heat transfer rate enhances.

In this study, shock wave laminar boundary layer interaction in a hypersonic flow past a cylindrically blunt fin mounted on a flat plate is studied using a viscous perfect gas model. The freestream Mach number and Reynolds number -based on the diameter of the cylindrical fin- is 14 and 8,000, respectively. Navier-Stokes and ideal gas equations are solved using an MPI code written in the C++ language by the authors. The code has been validated in previous studies[12] . Two separate sweep angles of the fin relative to the flat plate ($\Lambda = 0^0$ and 22.5^0) have been investigated to study the effect of the sweep angle on the shock wave boundary layer interaction. The heat transfer

DOI: 10.13009/EUCASS2017-65

on the blunt fin is compared with the experimental data for validation. Some results of these calculations have been presented before[13] .

Experiment

The experiment was conducted by Hiers *et al.*[10] where the shock wave laminar boundary layer interaction was studied in a hypersonic flow over a blunt fin. The model in this study consists of a flat plate with a rotatable cylindrical blunt fin (Figure 1). The blunt fin can rotate to form variety of sweep angles, including $\Lambda = 0^0$ and 22.5^0. The centerline heat transfer on the blunt fin has been measured to study the shock wave laminar boundary layer interaction in a hypersonic flow with freestream Mach number and Reynolds number -based on the diameter of the fin- at 14 and 8,000, respectively. The schematics of the model is presented in Figure 2, where all the lengths have been normalized by the diameter of the fin (D = 2.54 cm (1 in)).

The experiment was conducted in the NASA Ames 1-foot shock tunnel with its stagnation enthalpy and pressure at 10.5 MJ/kg and 290 atm, respectively. The non-equilibrium effects are reported to be negligible, as well as the enthalpy of the frozen degrees of freedom at the test section, which is less than 10% of the total enthalpy. The model is instantly exposed to the flow from the isothermal condition of the room temperature. The time-averaged heat transfer on the centerline of the fin is measured and normalized with the stagnation point heat transfer by Fay and Riddle's method[8] . The total uncertainty of the heat transfer measurements was reported to be less than ±20%. More information on the average flow parameters at the test section is presented in Table 1.

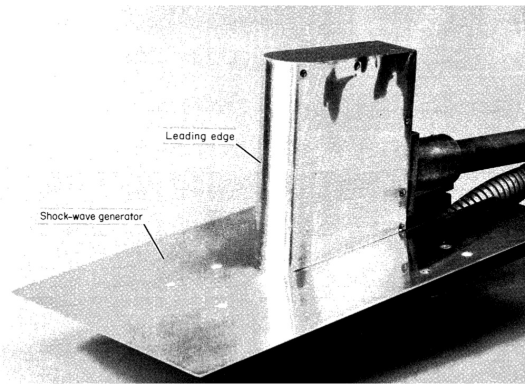

Figure 1: Experiment

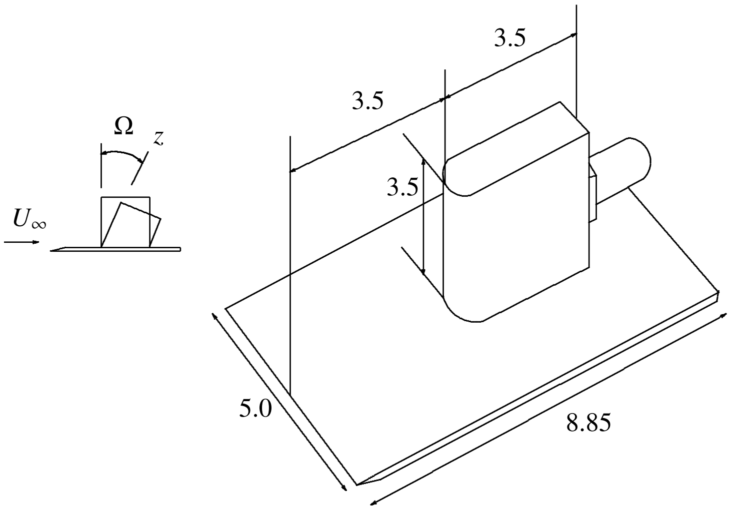

Figure 2: Schematics of the Model

Table 1: Experimental Condition[10]

Parameter	**Value**
Mach number	14
Reynolds number, $Re_d = \rho_\infty U_\infty D/\mu_\infty$	8,000
Stagnation pressure p_{st} (MPa)	29.38
Stagnation enthalpy h_0 (MJ/kg)	10.5
Velocity U_∞ (m/s)	4,270
Static temperature T_∞ (^{0}K)	195
Wall temperature T_w (^{0}K)	293
Diameter of the fin D (cm)	2.54
Sweep angle of the fin (Λ)	0^0, 22.5^0

DOI: 10.13009/EUCASS2017-65

Methodology

In this study, the experiment conducted by Hiers *et al.*[10] for two separate sweep angles of $\Lambda = 0^0$ and 22.5^0 is numerically simulated using a viscous perfect gas model. The Navier-Stokes equations coupled by the Ideal Gas Equation have been solved using an MPI code written in the C++ language by the authors. The code has been validated before using the analytical solution of the compressible Blasius problem and a two-dimensional shock wave boundary layer interaction[12]. The finite volume method is used to solve the unsteady equations, with the time integrated explicitly using the second order Runge-Kutta's method[9]. The inviscid flux algorithm of Roe's scheme[15,16] is used with second order primitive MUSCL algorithm[14] to reconstruct for pressure, temperature and the velocities. The molecular viscosity is calculated by the Sutherland's law scheme[17] and laminar Prandtl number is fixed at 0.72. All the flow parameters are normalized by the freestream values and the non-dimensional parameters are set at the experimental condition (Table 1).

The computational domain is decomposed to numerous zones to assign to different cores for calculation using the MPI code. The grid is structured and it has been created with a C++ code by the first author. Each boundary of each zone is labeled by an identification number to be recognized in the solver code. Both external and internal boundary conditions are implemented using some ghost cells at each boundary of each zone. The neighboring zones are recognized by matching identification numbers assigned in the grid and recognized in the solver code. The communication between each zone is conducted by the ghost cells at the internal boundaries with the recognized neighboring zones.

The initial computational domain is presented in Figure 3 with the no-slip isothermal boundary condition on the solid walls, which consist of the cylindrical blunt fin and the flat plate. Symmetry boundary condition is used for the vertical center-plane, top and rear boundaries, and zero-gradient boundary condition is implemented at the outflow, which is the right boundary. The left boundary, which represents the inflow, is fixed at the freestream condition. Due to high temperature gradient in hypersonic speeds for isothermal boundary condition, it is more numerically feasible to use the no-slip adiabatic boundary condition for the solid boundaries and use that solution as the new initial condition to solve with the no-slip isothermal boundary condition.

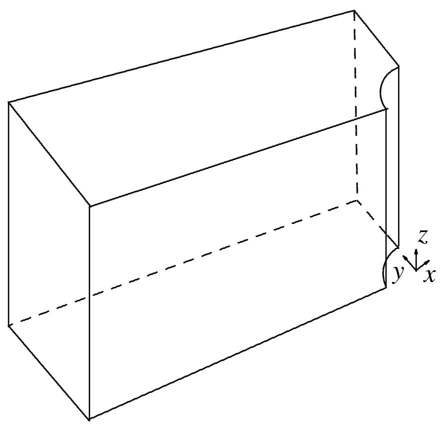

Figure 3: Initial Computational Domain

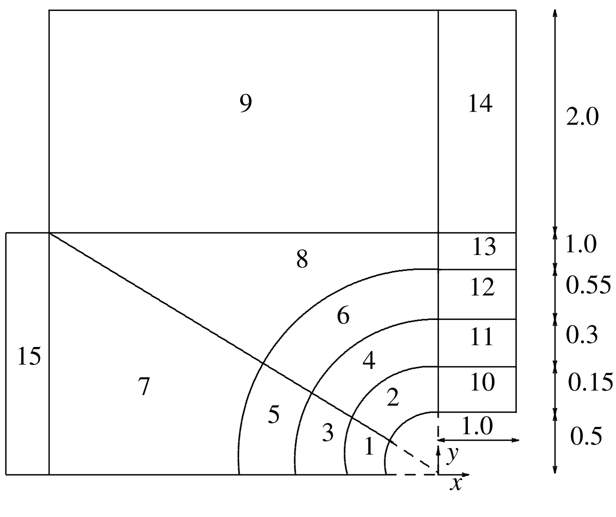

Figure 4: $z = 0$ Plane of the Computational Domain

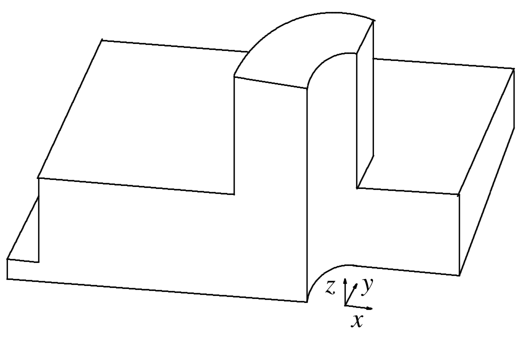

Figure 5: Computational Domain (0^0 Sweep Angle)

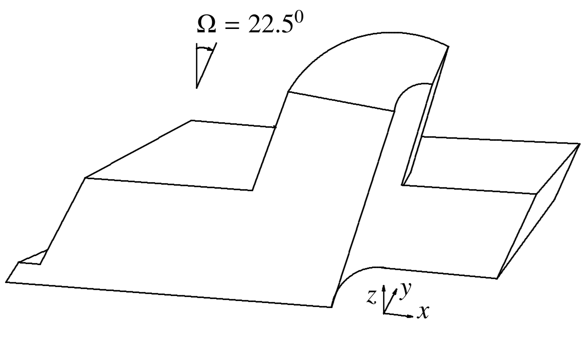

Figure 6: Computational Domain (22.5^0 Sweep Angle)

DOI: 10.13009/EUCASS2017-65

The calculations in the initial computational domain with a coarser grid gives us an approximation of the length of the separation region, boundary layer thickness and the location of the shock waves. This information helps us recognize unimportant zones with flow parameters fixed at the freestream condition. For later calculations those unimportant zones are omitted, leading to a finer grid with the same computational resources. Figures 5 and 6 present the schematics of the final computational domain for zero and 22.5^0 sweep angles, respectively. These grids consist of 127 zones, which are built layer by layer. Figure 4 presents the base of the first layer of the grid, with lengths normalized by the diameter of the cylindrical fin. The first layer of the mesh has the maximum number of the zones, with 15 zones.

The boundary layer at the outflow should be well-developed for the zero-gradient boundary condition to be accurate at that location. The reason for adding the zones 9 to 14 is that the boundary layer was not well-developed at the outflow boundary for the initial computational domain and it needed to be expanded further in the downstream direction. Moreover, the boundary layer cannot start at the beginning of the computational domain, since it would contradict the fixed boundary condition at that edge. Therefore, the zone number 15 was added with the symmetry boundary condition at the bottom. The boundary condition for the bottom boundaries of the zones 9 and 14 are symmetry, as well. No-slip isothermal boundary condition is applied on all the boundaries representing the solid walls of the cylindrical fin and the flat plate.

The information of the final mesh of the both sweep angles of 0^0 and 22.5^0 is presented in Table 2, with $\Delta_{\min,n}/D$, $\Delta_{\max,s}/D$ and $\Delta_{\min,t}/D$ representing the dimensionless minimum spacing in the radial, tangent in θ direction, and tangent along the centerline of the cylindrical fin, respectively.

Table 2: Details of the Grids (Ω = 0^0 and 22.5^0)

No. of real cells	$\Delta_{\min,n}/D$	$\Delta_{\min,s}/D$	$\Delta_{\min,t}/D$
17,462,500	0.0014	0.0056	0.0108

Results

A blunt shock wave forms upstream of the cylindrical blunt fin, which interacts with the boundary layer over the flat plate. The intense adverse pressure gradient from the blunt fin shock wave separates the boundary layer, creating a separated region with horseshoe vortices. The information of the adverse pressure gradient travels inside the subsonic region, moving the separation point to the upstream. The interaction of the shock wave with the boundary layer creates a complex flow structure. Figures 7 and 8 present the $\log_{10}(p/p_\infty)$ contours for the zero and 22.5 degree sweep angle cases, respectively. The separation point and the blunt fin shock wave are evident in the figures. The adverse pressure gradient imposed from the zero degree sweep angle fin is larger than that of the 22.5^0 case, leading to larger separation region for the zero degree sweep angle case. From the figures it is evident that the separation point for the zero degree sweep angle case is further upstream compared to the 22.5 degree case. The separated boundary layer reattaches to the fin and creates a localized high pressure at the reattachment point. It is evident from the figures that the maximum pressure created by the zero degree sweep angle interaction is higher than that of the 22.5^0 case.

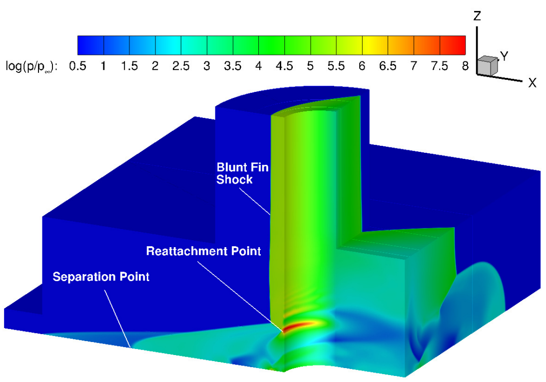

Figure 7: $\log_{10}(p/p_\infty)$, 0^0 Sweep Angle

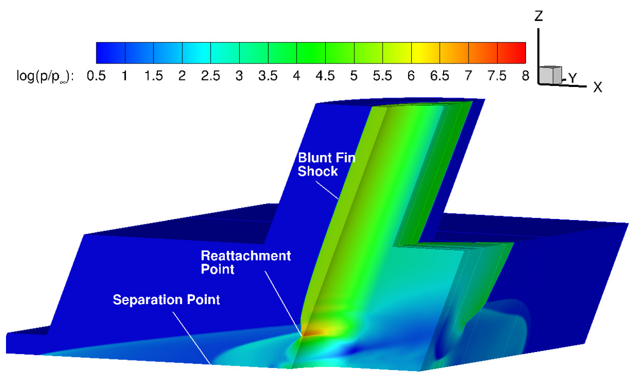

Figure 8: $\log_{10}(p/p_\infty)$, 22.5^0 Sweep Angle

Figures 9 and 10 present the Mach number contours and the sonic lines at the center-plane for the zero and 22.5 degree sweep angles, respectively. A boundary layer displacement shock wave forms over the boundary layer on the flat plate, with its angle only dependent on the freestream condition. A separation shock wave forms over the separated

DOI: 10.13009/EUCASS2017-65

region, which later interacts with the blunt fin shock wave. The separation region formed in the zero degree case is double the size of the separation region in the 22.5 degree case, due to higher adverse pressure gradient imposed from the fin in this case. As a result, the separation shock wave created in the zero degree case is formed further upstream and away from the plate compared to the 22.5^0 case. The separation shock wave in the 22.5^0 case is formed below the boundary layer displacement shock wave, leading to two separate shock/shock interactions; one of them is the weak interaction of the boundary layer displacement shock wave and the blunt fin shock wave, and the other is the stronger interaction of the separation and the resultant transmitted shock waves. However, in the zero degree case, the separation shock wave interacts the displacement thickness shock wave prior to intersecting the blunt shock wave.

Figures 11 and 12 present the static temperature contours normalized by the freestream static temperature at the center-plane for zero and 22.5 degree sweep angle cases, respectively. The increase in the temperature after the blunt fin shock wave is evident in both cases; however, due to cold isothermal boundary condition at the walls there is a sharp gradient of temperature close to the wall, leading to high heat transfer rate on the fin. Three and two horseshoe vortices are detected in the zero and 22.5 degree cases, respectively. Since the separation region in the zero degree case is double the size of the separation region in the 22.5 degree, more vortices are formed in this case. As the separated boundary layer reattaches the solid wall on the fin, it creates a thin layer with large gradient in flow parameters such as temperature. As a result, there is an extreme localized heat transfer rate at the reattachment point. Moreover, a reattachment shock wave forms at the reattachment point, creating a localized peak in pressure.

Figures 13 and 14 present the shadow-graph at the center-plane for the zero and 22.5 degree sweep angle cases, respectively. The boundary layer displacement, separation, reattachment, transmitted and blunt fin shock waves are evident from the figures. The faded rectangles and parallelograms do not have a physical representation and are the separate zones in the grid that the data visualization software (tecplot) could not blend well enough with the neighboring zones. The complex shock wave structure inside the separated region -specially for the zero degree sweep angle case- is evident from the figures. Figures 9 and 10 show distinct supersonic area inside the separated region, which are divided from the subsonic region with shock waves and slip-lines presented in the shadow-graphs. Another supersonic region is downstream the blunt fin, which contains compression and expansion waves. As the compression waves interact with the sonic line, they reflect as expansion waves. These expansion waves decrease the pressure on the fin as they interact with it. The expansion waves later reflect from the fin and interact with the sonic line and reflect from the sonic line as compression waves. The compression waves increase the pressure on the fin. As a result, we have oscillation of pressure on the fin as the expansion and compression waves interact with it. This phenomenon is evident from the plots of pressure on the centerline, which are presented in Figures 15 and 16. The high peak pressure is due to the interaction of the reattachment shock wave with the blunt fin. The strength of the reattachment shock wave and the peak pressure dramatically decreases for the 22.5 degree, comparing to the zero degree case.

The shock wave boundary layer interaction in this study is highly three-dimensional. Figures 17 and 18 present the shadow-graph of the three-dimensional shock wave surface in the computational domain for the zero and 22.5 degree sweep angle cases, respectively. The shock wave over the separated boundary layer and the blunt fin shock wave are evident from the figures. At the exit of the computational domain a complex structure of shock waves and slip-lines are captured (Figures 19 and 20). The blunt fin shock wave interacts with the boundary layer through the whole three dimensional domain and a three dimensional transmitted shock wave forms from this interaction. The transmitted shock wave is evident in the shadow-graphs at the end of the computational domain. Moreover, some streamlines at the vicinity of the center-plane are presented in Figures 21 and 22 for the zero and 22.5 degree sweep angle cases to show the structure of the streamlines inside the separated region in a three-dimensional perspective.

The surface heat transfer and skin friction lines on the solid surfaces for the zero and 22.5 degree cases are presented in Figures 23 and 24, respectively. The separation line and the reattachment point are detectable using the skin friction lines. The separation line is generated from a saddle point with two specific directions. The skin friction lines point towards the saddle point through one characteristic line, and point away from it through the other one. The separation line is evident from the characteristic line with skin friction lines pointing away from the saddle point. On the other hand, the reattachment point is a node with all the skin friction lines pointing away from that singular point. The maximum heat transfer is captured at the reattachment point for both of the zero and 22.5 degree cases.

Another characteristics of the results in this study is its unsteady oscillations, specially at the region where the transmitted shock wave interacts with the reattachment shock wave. A Mach reflection can form from the interaction of two strong shock waves by formation of a normal shock between the two interacting shock waves, which is called the Mach reflection. This phenomenon is captured at the interaction of the transmitted and the attachment shock waves. The Mach reflection oscillates leading to change in pressure and heat transfer close to the interaction region. Moreover, the slip-lines and the shock waves inside the separated boundary layer presented in the center-plane contours display temporal oscillations. The unsteady behavior rapidly subsides in the 22.5 degree, compared to the zero degree sweep angle case.

DOI: 10.13009/EUCASS2017-65

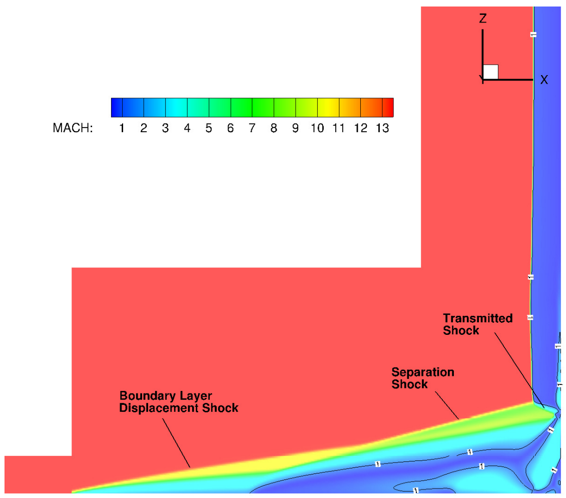

Figure 9: Mach Number, 0^0 Sweep Angle

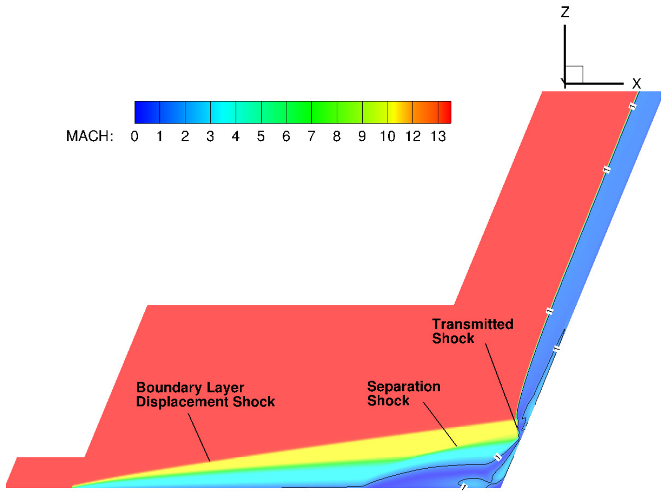

Figure 10: Mach Number, 22.5^0 Sweep Angle

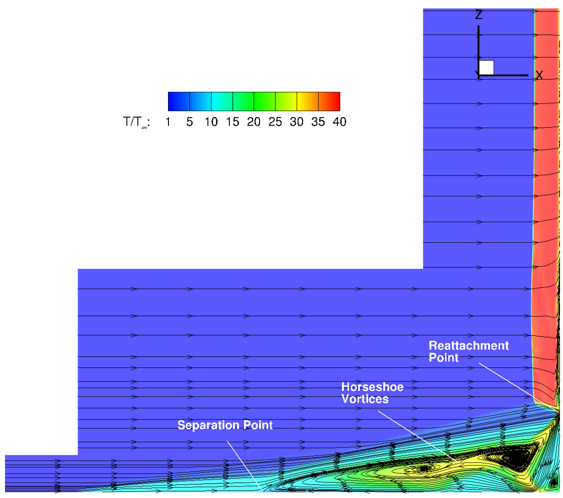

Figure 11: Static Temperature, 0^0 Sweep Angle

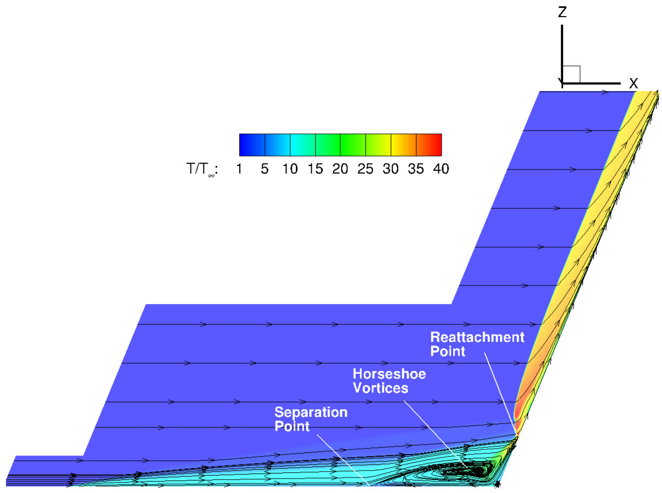

Figure 12: Static Temperature, 22.5^0 Sweep Angle

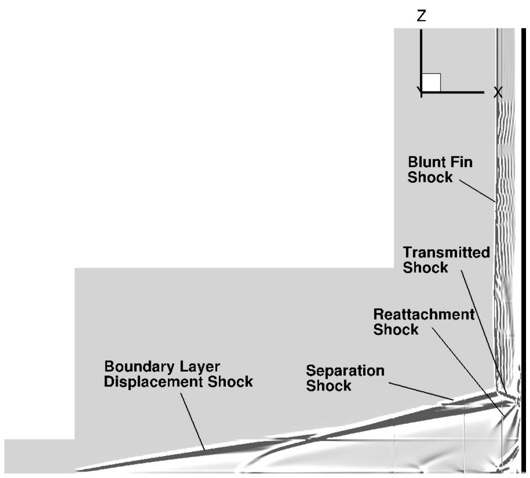

Figure 13: Shadow-graph, 0^0 Sweep Angle

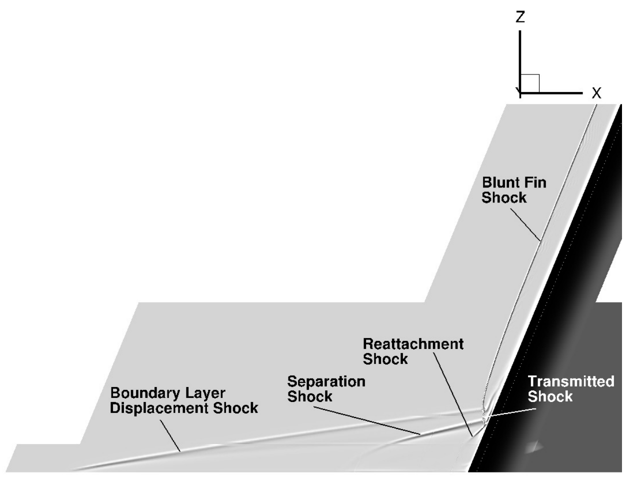

Figure 14: Shadow-graph, 22.5^0 Sweep Angle

DOI: 10.13009/EUCASS2017-65

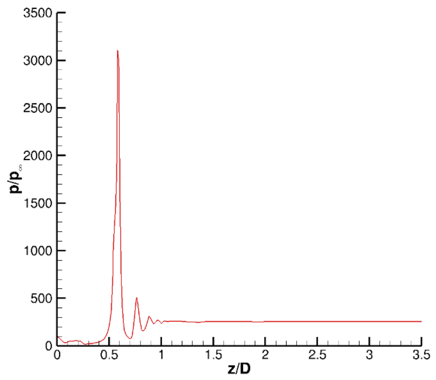

Figure 15: Pressure, 0^0 Sweep Angle

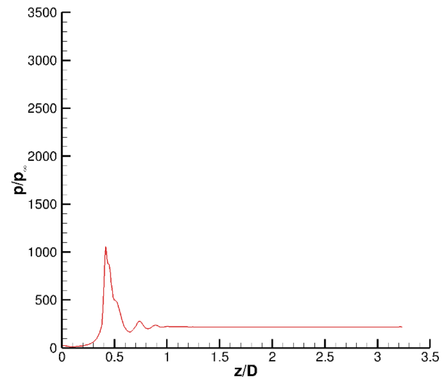

Figure 16: Pressure, 22.5^0 Sweep Angle

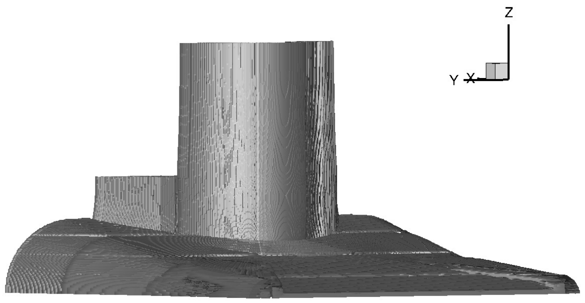

Figure 17: Shadow-graph, 0^0 Sweep Angle

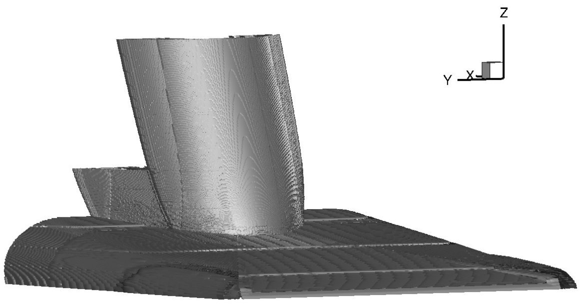

Figure 18: Shadow-graph, 22.5^0 Sweep Angle

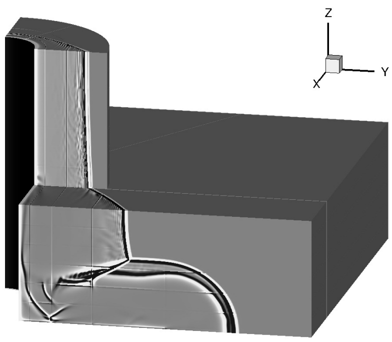

Figure 19: Shadow-graph, 0^0 Sweep Angle

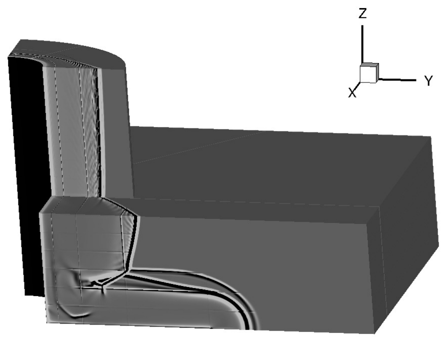

Figure 20: Shadow-graph, 22.5^0 Sweep Angle

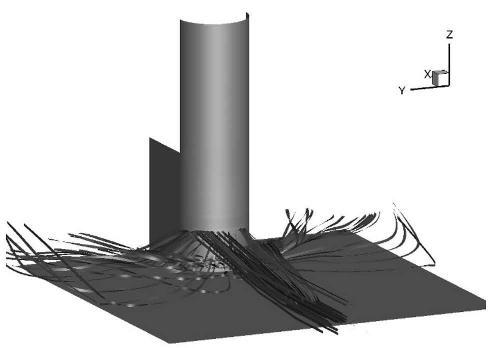

Figure 21: Streamlines, 0^0 Sweep Angle

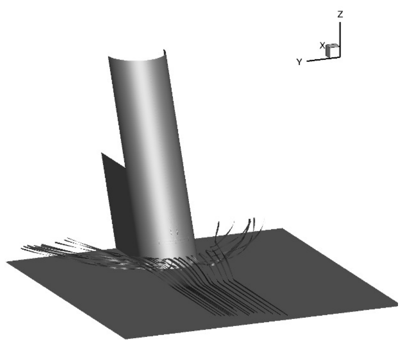

Figure 22: Streamlines, 22.5^0 Sweep Angle

DOI: 10.13009/EUCASS2017-65

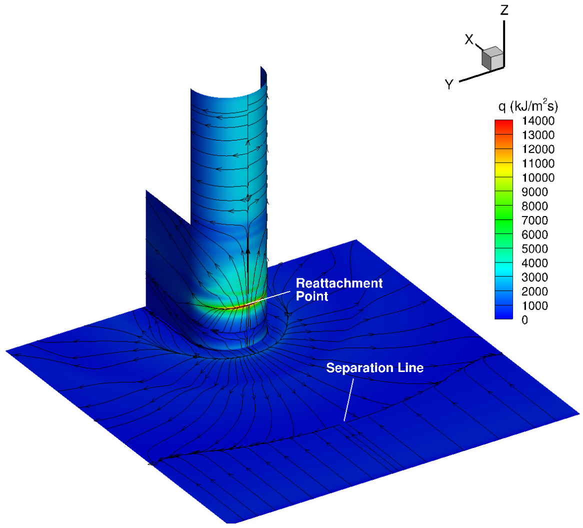

Figure 23: Surface Heat Transfer and Skin Friction Lines, 0^0 Sweep Angle

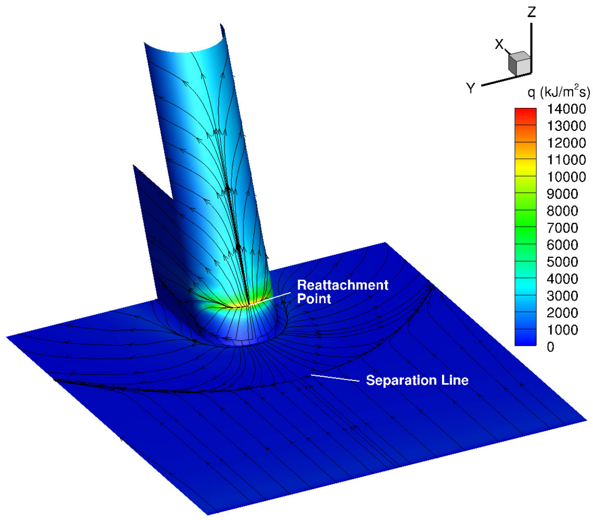

Figure 24: Surface Heat Transfer and Skin Friction Lines, 22.5^0 Sweep Angle

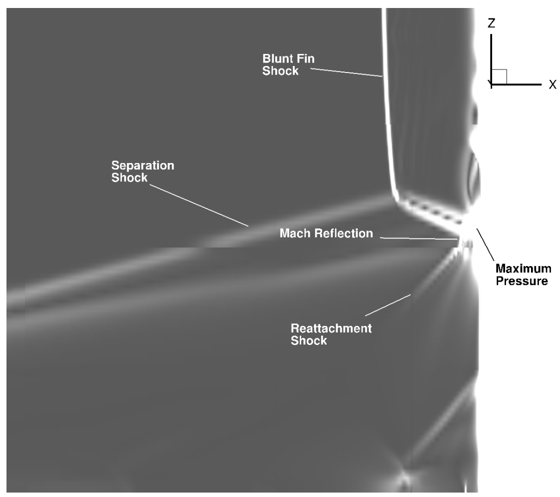

Figure 25: Schlieren Image, 0^0 Sweep Angle

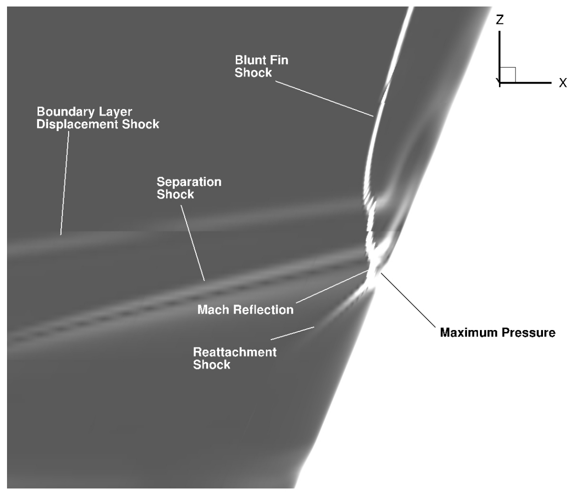

Figure 26: Schlieren Image, 22.5^0 Sweep Angle

Figures 27 and 28 present the pressure history normalized by the freestream pressure for the zero and 22.5 degree cases at z/D = 0.3016 and 0.4079 on the centerline, respectively. The heat transfer history for these two cases at the z/D = 0.3016 and 0.4079 on the centerline is presented in Figures 29 and 30, where the heat transfer is normalized by the freestream heat transfer calculated on the centerline of the fin away from the shock wave boundary layer interaction. The stagnation point heat transfer for the zero and 22.5 degree sweep angle cases are 3.1 and 2.8 MW/m^2, respectively. A great decay in the unsteady behavior has been captured in the 22.5 degree case, compared to the zero degree sweep angle case for both the pressure and heat transfer calculations. Discrete Fourier Transform analysis on multiple periods of oscillation has been used for the zero degree sweep angle case to study its unsteady behavior. The results show that the change of the dominant frequency of oscillation and the energy corresponding to that frequency is negligible. As a result, we can conclude that a statistically stationary solution for the zero degree sweep angle case has been reached.

Figures 31 and 32 present the experimental and numerical heat transfer on the fin for the zero and 22.5 degree sweep angle cases. The heat transfer for the experimental measurements are normalized by the method of Fay and Riddle[8] . The time-averaged heat transfer of the numerical calculations is compared with the experimental data for validation and good agreement with the experiment has been captured. The difference in the normalized peak heat transfer rate for the zero and 22.5 degree cases is negligible.

DOI: 10.13009/EUCASS2017-65

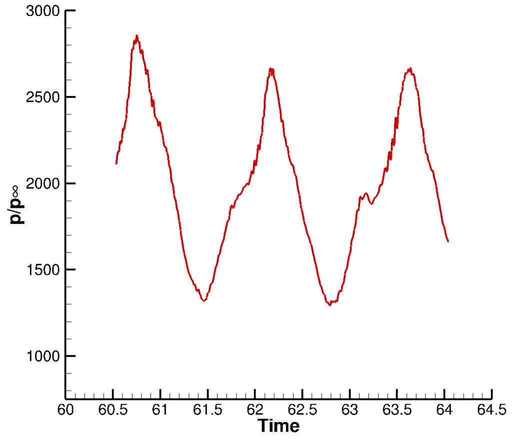

Figure 27: Pressure History at $z/D = 0.3016$, 0^0 Sweep Angle

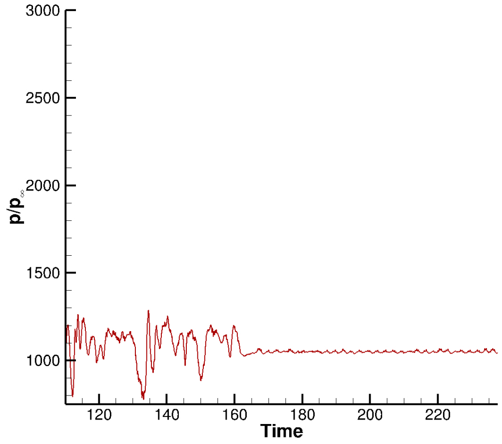

Figure 28: Pressure History at $z/D = 0.4079$, 22.5^0 Sweep Angle

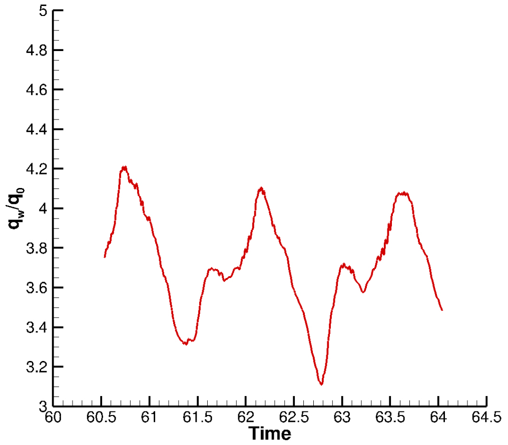

Figure 29: Heat Transfer History at $z/D = 0.3016$, 0^0 Sweep Angle

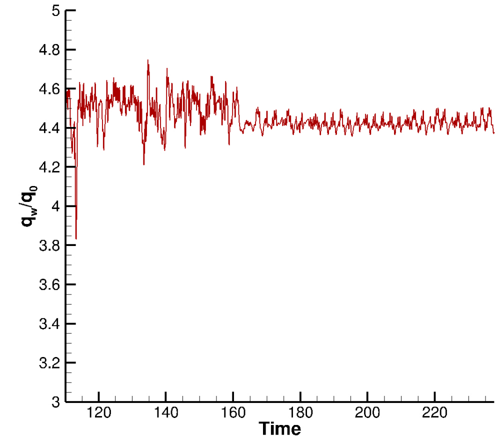

Figure 30: Heat Transfer History at $z/D = 0.4079$, 22.5^0 Sweep Angle

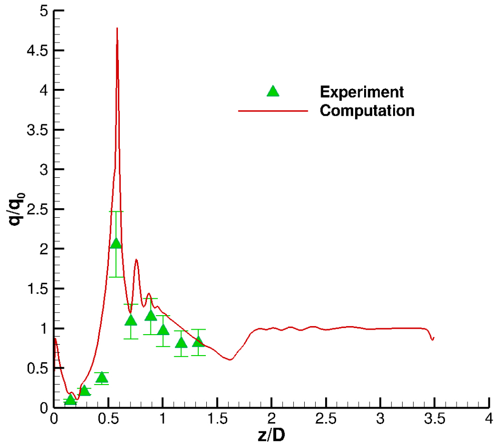

Figure 31: Heat Transfer, 0^0 Sweep Angle

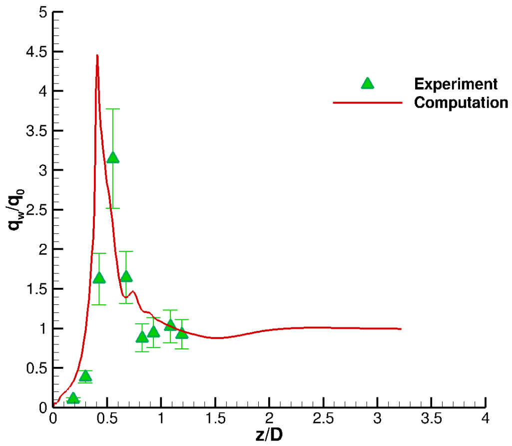

Figure 32: Heat Transfer, 22.5^0 Sweep Angle

DOI: 10.13009/EUCASS2017-65

Conclusion

The three dimensional shock wave boundary layer interaction in a laminar hypersonic flow is numerically investigated. A viscous perfect gas model is used and Navier-Stokes and Ideal Gas equations are solved by an MPI code written in the C++ language by the authors. A cylindrical blunt fin mounted on a flat plate at two separate sweep angles of zero and 22.5 degree is numerically simulated and the effect of the sweep angle on the interaction is studied. The blunt shock wave generated from the fin separates the boundary layer over the flat plate and creates a complex three dimensional shock wave boundary layer interaction. As the boundary layer reattaches on the solid surface over the fin, a reattachment shock wave forms creating a peak pressure on the solid wall. Moreover, the heat transfer rate reaches its maximum level at the reattachment point. Oscillations in the flow parameters and shock waves and slip-lines in the zero degree sweep angle case are captured. The Discrete Fourier Transform analysis show that the statistically stationary solution has been reached for the zero degree case, while the 22.5 degree case is steady. The time-averaged heat transfer is compared with the experimental data and good agreement with the experimental measurements validates our numerical calculations.

References

[1] Serge M Boldyrev, Volf Ya Borovoy, Andrey Yu Chinilov, Victor N Gusev, Serge N Krutiy, Irina V Struminskaya, Larissa V Yakovleva, Jean Délery, and Bruno Chanetz. A thorough experimental investigation of shock/shock interferences in high mach number flows. *Aerospace Science and Technology*, 5(3):167–178, 2001.

[2] Volf Y Borovoy, Ivan V Egorov, Arkady S Skuratov, and Irina V Struminskaya. Two-dimensional shock-wave/boundary-layer interaction in the presence of entropy layer. *AIAA Journal*, 51(1):80–93, 2012.

[3] R Bur and B Chanetz. Experimental study on the PRE-X vehicle focusing on the transitional shock-wave/boundary-layer interactions. *Aerospace Science and Technology*, 13(7):393–401, 2009.

[4] B Chanetz. Low and high enthalpy shock wave/boundary layer interactions around cylinder-flare models. In *Progress in Flight Physics*, volume 3, pages 107–118. EDP Sciences, 2012.

[5] Bruno Chanetz, Thierry Pot, Reynald Bur, Véronique Joly, Serge Larigaldie, Michel Lefebvre, Claude Marmignon, Ajmal K Mohamed, Jean Perraud, Daniel Pigache, et al. High-enthalpy hypersonic project at ONERA. *Aerospace Science and Technology*, 4(5):347–361, 2000.

[6] MC Coet. Etude experimentale de l'effet d'une couche d'entropie sur l'interaction onde de choc/couche limite en ecoulement hypersonique. *Rapport Complementaire, ONERA, Rapport Final no. 29/4362 AY*, 1992.

[7] MC Coet, B Chanetz, and JM Delery. Shock-wave boundary layer interaction with entropy layer effect in hypersonic flow. In *ONERA, Colloque sur les Ecoulements Hypersoniques, Garchy, France*, 1992.

[8] James A Fay. Theory of stagnation point heat transfer in dissociated air. *Journal of the Aerospace Sciences*, 25(2):73–85, 1958.

[9] Sigal Gottlieb and Chi-Wang Shu. Total variation diminishing Runge-Kutta schemes. *Mathematics of Computation of the American Mathematical Society*, 67(221):73–85, 1998.

[10] Robert S Hiers and William J Loubsky. Effects of shock-wave impingement on the heat transfer on a cylindrical leading edge. *NASA Technical Note*, 1967.

[11] Bibin John and Vinayak Kulkarni. Effect of leading edge bluntness on the interaction of ramp induced shock wave with laminar boundary layer at hypersonic speed. *Computers & Fluids*, 96:177–190, 2014.

[12] Mahsa Mortazavi and Doyle D Knight. Shock Wave Boundary Layer Interaction in a Hypersonic Laminar Flow on a Hollow Cylinder Flare. AIAA Paper 2016-0351, American Institute of Aeronautics and Astronautics, 2016. doi:10.2514/6.2016-0351.

[13] Mahsa Mortazavi and Doyle D Knight. Shock Wave Laminar Boundary Layer Interaction at a Hypersonic Flow Over a Blunt Fin-Plate Junction. AIAA Paper 2017-0536, American Institute of Aeronautics and Astronautics, 2017. doi:10.2514/6.2017-0536.

[14] James J Quirk. An alternative to unstructured grids for computing gas dynamic flows around arbitrarily complex two-dimensional bodies. *Computers & Fluids*, 23(1):125–142, 1994.

DOI: 10.13009/EUCASS2017-65

[15] Philip L Roe. Approximate Riemann solvers, parameter vectors, and difference schemes. *Journal of Computational Physics*, 43(2):357–372, 1981.

[16] Philip L Roe. Characteristic-based schemes for the Euler equations. *Annual Review of Fluid Mechanics*, 18(1):337–365, 1986.

[17] William Sutherland. The viscosity of gases and molecular force. *The London, Edinburgh, and Dublin Philosophical Magazine and Journal of Science*, 36(223):507–531, 1893.

[18] AB Swantek and JM Austin. Flowfield establishment in hypervelocity shock-wave/boundary-layer interactions. *AIAA Journal*, 53(2):311–320, 2014.